
UNDERSTANDING MULTI-LAYERED TRANSMISSION MATRICES

Anat Levin, Marina Alterman

Department of Electrical and Computer Engineering, Technion, Haifa, Israel,
 anat.levin@ee.technion.ac.il

ABSTRACT

Transmission matrices, mapping the propagation of light from one end of the tissue to the other, form an important mathematical tool in the analysis of tissue scattering and the design of wavefront shaping systems. To understand the relationship between their content and the volumetric structure of the tissue, we wish to fit them with multi-slice models, composed of a set of planar aberrations spaced throughout the volume. The number of layers used in such a model would largely affect the amount of information compression and the ease in which we can use such layered models in a wavefront-shaping system. This work offers a theoretical study of such multi-layered models. We attempt to understand how many layers are required for a good fit, and how does the approximation degrade when a smaller number of such layers is used. We show analytically that transmission matrices can be well fitted with very sparse layers. This leads to optimistic predictions on our ability to use them to design future wavefront shaping systems which can correct tissue aberration over a wide field-of-view.

1 Introduction

Transmission matrices are a mathematical tool used to model the propagation of coherent light from one end of a scattering medium to the other. Since light propagation is linear, by recording the propagation of a set of basis wavefronts through the medium, one can predict the propagation of all their linear combinations. Transmission matrices are a central mathematical tool in biomedical engineering and physics. They are used to study the statistical properties of scattering such as the memory effect Schott et al. [2015], Osnabrugge et al. [2017], Alterman et al. [2021], Bar et al. [2021], Andreoli et al. [2015], in the design and analysis of wavefront shaping algorithms Rotter and Gigan [2017], Popoff et al. [2011], Boniface et al. [2020], Gigan et al. [2022], Zhu et al. [2022], Aizik et al. [2022], Aizik and Levin [2024], Yeminy and Katz [2021], Feng et al. [2023], Kang et al. [2015], Blochet et al. [2019], Metzler et al. [2017], Sharma et al. [2020], Lee et al. [2023], Baek et al. [2023], Zhang et al. [2024], and in diffraction tomography tissue reconstructions Horstmeyer et al. [2016], Chowdhury et al. [2019], Chen et al. [2020], Zhou and Horstmeyer [2020], Kang et al. [2023], Liu et al. [2022], Xue et al. [2022], He et al. [2024], Kamilov et al. [2015], Sun et al. [2018].

Transmission matrices are usually 4D entities capturing the relationship between a 2D family of incoming wavefronts to the 2D outgoing wavefronts they generate on the other side of the volume. To relate their content to the 3D structure of the scattering volume one can approximate them with a multi-slice model, where the scattering volume is approximated as a set of planar aberrations, assuming free space propagation between layers.

This approximation model has multiple applications. First, 4D transmission matrices are very large objects and by approximating them with the 3D layer structure we obtain significant compression. Second, multi-slice models provide an understanding of the 3D structure. A third application is improving wavefront shaping systems. Currently, one of the main challenges in large scale adaptation of wavefront shaping algorithms is the fact that a single planar SLM can correct tissue aberrations in a very local window Osnabrugge et al. [2017], Alterman et al. [2021]. While we can run a wavefront estimation algorithm like that of Boniface et al. [2020], Aizik et al. [2022], Aizik and Levin [2024] multiple times in many local windows, in order to smartly interpolate between local corrections one should recover the structure of the refractive indices at any point in the volume, as done by diffraction tomography algorithms. Moreover, since the scattering happens through a 3D volume, to fully correct aberration over a large field of view the correction element should also be a volumetric hologram rather than a planar SLM. Volume holograms are usually

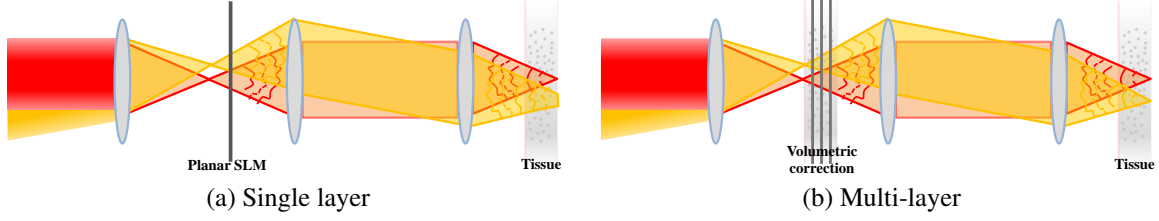


Figure 1: **Layered wavefront shaping:** (a) A single planar SLM can correct aberration at a local spot (see red beam) but if we scan it with illumination tilted toward a different spot it will aberrate when propagating through the tissue (yellow beam does not converge to a narrow spot inside the tissue). (b) The field of view of the correction can possibly be extended with a multi-layer correction. The goal is that multiple beam passing through the SLMs will aberrate in a way which is the conjugate of the aberration in the tissue, so with successive propagation through the tissue itself it focuses into a spot. The figure illustrates two beams illuminating the same volumetric correction, and both focus into a sharp spot behind the tissue.

created using photographic emulsions or photo-refractive crystals, but these cannot be programmed as easily as an SLM. An alternative is to approximate the volumetric correction with a small number of planar SLMs positioned such that each of them is conjugate to a different plane inside the scattering volume. When such a multi-layer correction is placed at the optical path, one could scan it with a focused beam, at the speed of a Galvo mirror, as done by a standard confocal microscope, see Fig. 1. The beam would aberrate when moving through the multi-layer correction, but this aberration would be the conjugate of the aberration that a focused beam would pass through the tissue, so that the two aberrations cancel each other, and the beam focuses into a spot inside the tissue. The location of this spot can be shifted very fast by a Galvo mirror *without changing the content of the correction SLMs*. Indeed, multi-conjugate Adaptive Optics systems using two AO surfaces rather than one were introduced by Thauung et al. [2009], wei Wu and Cui [2015], Laslandes et al. [2017], Furieri et al. [2023], demonstrating empirically that the two plane correction can significantly extend the corrected field of view. These systems were aimed at correcting aberrations in the optical path rather than 3D scattering in the tissue, but they provide encouraging deviance for the potential of multi-layer corrections.

The goal of this research is to study multi-slice models. We aim to understand how many planar layers we need to actually approximate a 4D transmission matrix, and how does the accuracy of the approximation degrade if we use a sparser sampling of such planes.

The straightforward answer to this question is to say that the spacing between layers should match the axial resolution of the microscope. For example, using a $\text{NA} = 0.5$ objective at wavelength 500nm , we get that the spacing between layers should be lower than $2\mu\text{m}$. Handling a modest tissue thickness of, e.g. $200\mu\text{m}$ already requires 100 slices for a valid approximation. Such a large number of layers is prohibitive for computational diffraction tomography reconstruction algorithms, and it is clearly impractical to build a physical wavefront shaping system with so many planar SLMs. However, empirical evidence in diffraction tomography research suggests that good results can be obtained with a significantly lower number of layers. For example, Kang et al. [2023] corrects aberration through a few hundred microns of tissue using only 5 layers.

Our goal in this research is to explain this empirical observation. To this end, we offer a thorough analysis of the frequency content of transmission matrices, combining the forward scattering nature of biological tissue with the structure of the missing cone. We show that while the missing cone structure is known as one of the fundamental limitations of 3D microscopy, in the context of transmission matrices the limitations turn into an advantage. Due to the missing cone structure, a lot of the frequencies of the volumetric aberration do not participate in the transmission matrix, and therefore the transmission matrix can be approximated with a fairly low number of layers, well below the Nyquist limit. Finally, we investigate empirically the quality of the multi-slice approximation using real transmission matrices captured in the lab as well as synthetic transmission matrices simulated using accurate scattering models. We show that even though such transmission matrices include backward and sideward scattering which are not accounted for by multi-slice models, real transmission matrices can be well-fitted with a small number of planar aberration layers. We also study the implications of these findings to wavefront shaping systems and show that a wavefront shaping system composed of a small number of 2-3 SLM layers can largely accelerate the correction of wide-field-of-view images.

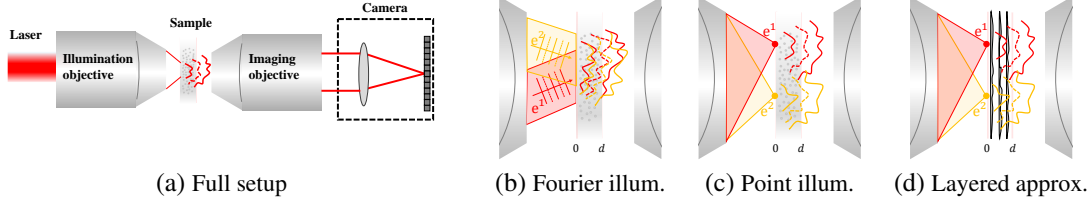


Figure 2: **Setup for transmission matrix acquisition:** (a) A setup for transmission matrix imaging where a set of basis illuminations at the back of the sample propagate through the volume and the scattered wavefronts are measured by a camera at the other end. In (b,c) we zoom on the sample illustrating two possible illumination bases. (b) A set of directional wavefronts (Fourier basis). (c) A set of wavefronts focused to points at the edge of the volume (primal basis). Both transmission matrices can be related by a simple Fourier transform. (d) A multi-slice model approximates the volumetric scattering with a set of planar aberrations.

2 Results

Problem formulation

Imaging setup: For simplicity, the following derivation considers coherent scalar waves, ignoring polarization. In Fig. 2(a) we visualize a setup for transmission matrix acquisition. A scattering medium, such as tissue, is illuminated by a coherent source \mathbf{e}^k at one side of the medium. After propagating through the medium the resulting coherent wavefront \mathbf{t}^k is recorded. The illumination is translated and multiple wavefronts are recorded and stored as columns of a transmission matrix \mathcal{T} .

The transmission matrix: Since the propagation of coherent light is linear, if we want to predict the propagation of any wavefront \mathbf{u} , we simply express it as a superposition of the recorded incoming illuminations $\mathbf{u} = \sum_k \mathbf{u}(k) \mathbf{e}^k$, where $\mathbf{u}(k)$ are complex scalars, and multiply it with the transmission matrix, to predict $\mathcal{T}\mathbf{u}$. The illumination wavefronts \mathbf{e}^k can be selected at different bases. For example, the illumination can be translated at the Fourier plane and then the wavefronts illuminating the sample are plane waves at different angles (Fig. 2(b)). Alternatively one can focus the light to a point at the back plane of the sample (Fig. 2(c)). This configuration is more appropriate for wavefront shaping algorithms whose goal is to recover wavefronts focusing inside the tissue and not far behind it. In both cases, however, the illuminations we can create are limited by the numerical aperture of the illuminating objective, which we mark here as \mathbf{NA} . Similarly, the scattered wavefront is measured via an imaging objective with a bounded \mathbf{NA} , for simplicity we assume the same numerical aperture is used in the illumination and imaging sides. This \mathbf{NA} would serve as a central component in the results derived below. For simplicity of resulting equations, for the rest of this manuscript we assume the imaging and illumination objectives are focused at the same plane, such that if we would remove the scattering sample and image the sources directly we would see the \mathbf{e}^k illuminations as sharp spots on the sensor plane. That is, if we use directional illuminations, we also measure the Fourier transform of the scattered waves, namely place the sensor at the Fourier plane of the imaging objective. If we use point sources at the back plane of the medium, we also focus the imaging objective at the same plane (that is, the imaging objective at the front of the tissue attempts to focus at the back plane), so we measure a speckle image of a relatively small support.

Range and resolution: We assume that in the primal basis the illuminators are spaced within an area of $\Omega_p \times \Omega_p$, and we sample them at the Nyquist resolution, so for an illumination wavelength λ they are separated by a pitch $\Delta_p = \lambda/(2\mathbf{NA})$. Equivalently, if we express them in the Fourier domain, we illuminate the sample with plane waves of the form

$$\mathbf{e}(\mathbf{r}) = e^{2\pi i(\bar{\kappa} \cdot \mathbf{r})} \quad (1)$$

where \mathbf{r} is a point inside the 3D volume and $\bar{\kappa} = \frac{1}{\lambda} \bar{\omega}$ where λ is the wavelength and $\bar{\omega}$ is a unit norm direction vector, i.e. the last entry of the direction vector ω_z is $\omega_z = \sqrt{1 - (\omega_x^2 + \omega_y^2)}$. For simplicity of notation, we assume the index of refraction of the leading medium is 1. We can only use illumination direction inside the numerical aperture $\sqrt{\omega_x^2 + \omega_y^2} \leq \mathbf{NA}$ (or equivalently $\sqrt{\kappa_x^2 + \kappa_y^2} \leq \Omega_f$ with $\Omega_f = \mathbf{NA}/\lambda$). To sample the transmission matrix at the Nyquist pitch, the κ_x, κ_y components of the illumination are sampled by the Nyquist pitch $\Delta_f = 1/2\Omega_p$.

With the above sampling scheme, the transmission matrices at the Fourier and primal bases are related by a simple Fourier transform $\mathcal{T}^p = \mathcal{F}^T \mathcal{T}^f \mathcal{F}$. We perform most of our analysis using the Fourier representation, but the transmission matrices we use in numerical simulations are in the primal domain. Since Fourier and primal transmission matrices are related by an orthonormal transformation, minimizing the fitting error in one basis or the other is equivalent.

The multi-slice model: The relation between an incoming illumination to an outgoing one is determined by the solution to a wave equation which takes into account the variation in refractive index inside the sample. Rather than a fully continuous model, in a multi-slice model we approximate the volume with a set of planar aberrations, separated by small z distances Δ_z , where we have free space propagation between layers, as in Fig. 2(d). Mathematically this can be described as

$$\mathcal{T}(\rho_1, \dots, \rho_M) = \mathcal{P}_O \mathcal{D}(\rho_M) \dots \mathcal{P}_{\Delta_z} \mathcal{D}(\rho_2) \mathcal{P}_{\Delta_z} \mathcal{D}(\rho_1), \quad (2)$$

where $\rho_m(x, y)$ is the 2D aberration of the m th layer and $\mathcal{D}(\rho_m)$ is a diagonal matrix performing element-wise multiplication of the incoming wavefront by the aberration. \mathcal{P}_{Δ_z} describes free space propagation between layers at distance Δ_z , which is essentially a convolution with a spherical wavefront. Finally \mathcal{P}_O propagates the wavefront in free space from the tissue boundary, via the lenses, to the camera sensor.

As the propagation operators $\mathcal{P}_{\Delta_z}, \mathcal{P}_O$ are known and \mathcal{D} is diagonal, an $N \times N$ transmission matrix has only $N \cdot M$ degrees of freedom. Usually $M \ll N$ and this approximation can largely reduce the degrees of freedom in the transmission matrix.

Our goal in this work is to understand what plane spacing Δ_z will facilitate a good representation of \mathcal{T} , and how would this approximation degrade when we use sparser sampling.

When the scattering is weak it is common to approximate the aberration layers as

$$\rho_m(x, y) = \mu + \delta\rho_m(x, y) \quad (3)$$

where μ is a scalar whose magnitude is a bit smaller than 1, encoding the ballistic portion of the light which passes through the layer without aberration, and the magnitude of the aberration is significantly smaller than the ballistic term $|\delta\rho_m(x, y)| \ll |\mu|$. When the scattering is weak most of the energy does not scatter more than once. It is therefore common to consider a first order approximation to the transmission matrix (often known as the single scattering or first-Born approximation), which reduces to

$$\begin{aligned} \mathcal{T}(\delta\rho_1, \dots, \delta\rho_M) \approx & \mu^M \mathcal{P}_O \mathcal{P}_{M\Delta_z} + \\ & \mu^{M-1} \sum_{m=1}^M \mathcal{P}_O \mathcal{P}_{(M-m)\Delta_z} \mathcal{D}(\delta\rho_m) \mathcal{P}_{m\Delta_z} \end{aligned} \quad (4)$$

The full light propagation in Eq. (2) includes multiplication of the different aberrations and hence the transmission matrix is highly nonlinear. In contrast, the advantage of the weakly scattering model in Eq. (4) is that the resulting transmission matrix is a linear function of the aberration layers. This linear approximation significantly simplifies analysis.

Diffraction tomography algorithms such as Chowdhury et al. [2019] capture a subset of columns from the transmission matrix and use gradient descent optimization to seek layers ρ_1, \dots, ρ_M which best explain the measured wavefronts. We will use a similar optimization scheme below, when trying to find a multi-slice representation for a given transmission matrix. We will then investigate the accuracy of such approximations and analyze their usage for wavefront shaping.

Sampling theory for transmission matrices

Nyquist sampling and the missing cone

We start by considering the case of weakly scattering volumes which, as in Eq. (4), can be reasonably approximated by considering the component of light that scattered once. We also assume the transmission matrix is sampled over a very wide support Ω_p . We discuss the implications of multiple scattering and limited supports in subsequent sections.

We denote by $n(\mathbf{r})$ the difference between the refractive index at a 3D position \mathbf{r} in the volume to that of the leading medium around it. We denote its 3D Fourier transform by $\hat{n}(\boldsymbol{\kappa})$.

We start by considering the Fourier representation of the transmission matrix, where it is illuminated and measured by plane waves. Using the weakly scattering (first-Born) approximation, the wavefront scattering toward direction $\bar{\omega}^v$ when illuminated by an incoming plane wave at direction $\bar{\omega}^i$ is proportional, up to a multiplicative factor, to Horstmeyer et al. [2016]:

$$\propto \int n(\mathbf{r}) e^{2\pi i(\bar{\kappa}^i - \bar{\kappa}^v) \cdot \mathbf{r}} d\mathbf{r}, \quad (5)$$

with $\bar{\kappa}^v = 1/\lambda\bar{\omega}^v$, $\bar{\kappa}^i = 1/\lambda\bar{\omega}^i$. This implies that effectively an entry of the transmission matrix is a sample from the 3D Fourier transform of the volume at frequency $\boldsymbol{\kappa} = \bar{\kappa}^i - \bar{\kappa}^v$. Note that throughout this paper we use bars $\bar{\omega}, \bar{\kappa}$ to denote vectors with norm constraints, and use normal bold fonts to denote standard 3D vectors, such as frequencies $\boldsymbol{\kappa}$

in the 3D spectrum. Recalling that the illumination and viewing directions are limited by an aperture of width \mathbf{NA} , the subset of 3D frequencies captured by the transmission matrix occupies only a butterfly shape, and the rest of the cone is missing, see illustration in Fig. 3(a). Using paraxial approximation it can be shown Mertz [2019] that the range of frequencies which can be generated is

$$|\kappa_z| \leq \mathbf{NA}|\kappa_{xy}| - \frac{\lambda}{2}|\kappa_{xy}|^2 \quad \text{with} \quad |\kappa_{xy}| = \sqrt{\kappa_x^2 + \kappa_y^2}. \quad (6)$$

The missing cone problem limits the ability of microscopes to perform optical sectioning. This is also a serious problem for diffraction tomography algorithms aiming to recover the 3D structure of the refractive index $\mathbf{n}(\mathbf{r})$ from columns of the transmission matrix, since many of the frequencies of the volume cannot be measured, the recovered volume is often degraded. We argue that in the context of transmission matrices the missing cone problem turns into an advantage. The fact that the transmission matrix only captures a limited range of frequencies allows us to approximate it with fewer samples as derived below.

Minimal sampling: Our goal is to approximate a transmission matrix with layers. We start by asking what spacing between layers will allow an exact reconstruction of the transmission matrix. If we approximate the volume $\mathbf{n}(\mathbf{r})$ with a set of planes we essentially sample a continuous signal. Classical Nyquist theory states that if we sample a signal at intervals of Δ_z , its Fourier transform includes replicas spaced by $\Lambda = 1/\Delta_z$. To achieve a good reconstruction, we want replicas to happen only in areas of the spectrum that the transmission matrix does not sample. Since the κ_x, κ_y components of our illuminations are limited by the aperture $|\kappa_{xy}| \leq \Omega_f$, and given the butterfly shape in Eq. (6) the κ_z frequencies we need to maintain are bounded to

$$|\kappa_z| \leq \frac{\mathbf{NA}\Omega_f}{2}. \quad (7)$$

Therefore, for an error free reconstruction the replicas spacing should satisfy

$$\Lambda^* = \mathbf{NA}\Omega_f, \quad (8)$$

and we get that the minimal sampling pitch is bounded by

$$\Delta_z^* = \frac{1}{\mathbf{NA}\Omega_f} = \frac{\lambda}{\mathbf{NA}^2}. \quad (9)$$

For a scattering layer of thickness d , the number of required layers is:

$$M^* = \frac{d \cdot \mathbf{NA}^2}{\lambda}. \quad (10)$$

For typical numbers of an illumination wavelength $\lambda = 0.5\mu m$ and $\mathbf{NA} = 0.5$ we get that the plane spacing should be relatively small, and $\Delta_z \leq 2\mu m$. For a modest tissue thickness of $d = 200\mu m$ we will need $M = 100$ planes. This large number of planes is challenging for many numerical algorithms which attempt to find a multi-slice approximation. If our goal is to build a volumetric wavefront-shaping device with multiple SLMs, clearly such a large number of SLMs is unrealistic. However, empirical evidence in previous research, e.g. Kang et al. [2023] suggests that usually good reconstruction can be obtained with much fewer layers. Below we explain this finding. By considering the structure of the missing cone, and the fact that tissue is forward scattering we show that in practice one can get a good approximation to the transmission matrix with much lower M values.

Approximation error with sparse multi-slice samples

For thick samples the number of layers required to accurately fit a transmission matrix, as predicted by Eq. (9), may be very high. In many practical applications we may actually want to approximate our transmission matrices with fewer layers, at the price of some reconstruction error. Our goal is to understand how the reconstruction error is scaled as a function of the number of layers, or as a function of the spacing between them.

Consider a scattering sample of thickness d , which we try to approximate using $M < M^*$ layers separated by $\Delta_z = \frac{d}{M}$. We denote by \mathcal{E}_M the reconstruction error of a given captured transmission matrix with the best M layers

$$\mathcal{E}_M = \min_{\rho_1, \dots, \rho_M} \|\mathcal{T}_{\text{exact}} - \mathcal{T}(\rho_1, \dots, \rho_M)\|^2. \quad (11)$$

Our goal is to show that \mathcal{E}_M decays relatively fast with M and we can get a reasonable approximation to the transmission matrix even if the number of layers is significantly lower than the exact prediction in Eq. (10). This is a result of two main properties: (i) The fact that the volumes describing realistic tissue samples have more energy in the low

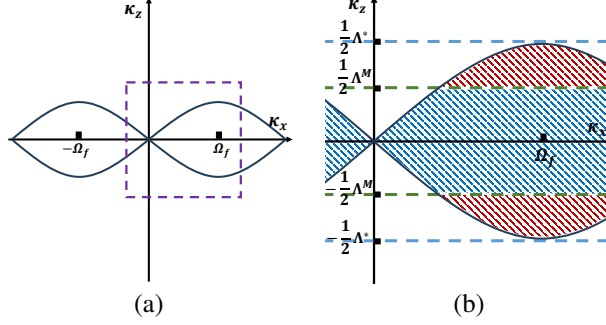


Figure 3: **Spectrum structure:** (a) an $x - z$ slice out of the spectrum of $\hat{n}(\omega)$. Entries of a weakly-scattering transmission matrix limited by an aperture \mathbf{NA} only lie inside the butterfly area. (b) zooming on the center right area of (a) (purple square). Assuming the ω_z axis is cut at $\pm \frac{1}{2} \Lambda^M$, the transmission matrix entries inside the dashed blue area are maintained, and the entries in the dashed red area are lost.

frequencies. (ii) The structure of the missing cone implies that, in any case, a significant portion of the spectrum is not sampled by the transmission matrix.

To understand this consider a naive selection of M layers ρ_1, \dots, ρ_M . Rather than actually solving an optimization problem, we use the ground truth volume $\hat{n}(\kappa)$, and simply set to zero any frequency content of the refractive volume $\hat{n}(\kappa)$ at κ_z values larger than the possible Nyquist range

$$\Lambda^M = \frac{1}{\Delta_z} = \frac{\lambda M}{d}, \quad (12)$$

and we then Fourier transform $\hat{n}(\kappa)$ to $n(\mathbf{r})$ and sample planes at spacing $\Delta_z = d/M$. The error of this approximation is basically the integral of content above the cut-off Λ^M . Since according to Eq. (12), the cut-off frequency Λ^M scales linearly with the number of layers, the portion of the spectrum which is lost by this low pass operation scales linearly with the number of layers M . Thus, the naive answer is that the error of a multi-slice approximation decays linearly with M . In practice we show below that the error decays much faster, since *large areas from the 3D spectrum of the sample are anyway not used by the transmission matrix*.

To gain intuition consider Fig. 3(b). We note that the butterfly shape is such that low 2D frequencies (i.e. low $|\kappa_{xy}|$), also span less content along the κ_z axes, and hence these frequencies are not lost even with low bandwidths Λ^M . For the higher $|\kappa_{xy}|$ frequencies, the lower κ_z part, marked in dashed blue in Fig. 3(b) is preserved, while the higher portion marked in red is lost.

Another important property of tissue is that its refractive index is locally smooth, and therefore if we look at its spectrum, we have much more energy in low frequencies than in high ones. Therefore, in the red areas of Fig. 3(b) which are not sampled by the transmission matrix there is less energy than in the lower frequencies. Therefore, despite the fact that the multi-slice approximation sacrifices such frequencies, not much energy is being lost.

In most cases, it is hard to give analytic formulas for the decay of \mathcal{E}_M as a function of M . We can derive analytic prediction in a simplified model where we assume that the spectrum of $\hat{n}(\kappa)$ has random values which are sampled from a uniform distribution for any frequency below a cutoff Ω_n (i.e. any frequency satisfying $\|\kappa\| \leq \Omega_n$), and zero content outside this band. Under this model we can prove that \mathcal{E}_M decays at least *quadratically* fast with M . This is a non-trivial result since the cut off frequency Λ^M scales only *linearly* with M , see Eq. (12). Thus, if we just rely on Nyquist theory and compute the energy of the spectrum above the cut-off frequency, we expect the error to decay linearly with M . The fact that the error decays quadratically with M results from the butterfly structure. We formulate here the result and prove it in the supplementary file. However, we emphasize that this result uses the over-simplified assumption of a uniform content in $\hat{n}(\kappa)$. In numerical simulation we see that this result is over-pessimistic, and with more realistic forward scattering volumes, the decay of \mathcal{E}_M is significantly faster than a quadratic function.

Claim 1 *The reconstruction error of a transmission matrix corresponding to a weakly scattering volume with a uniform spectrum, is bounded by*

$$\mathcal{E}_M \leq \left(\frac{M^* - M}{M^*} \right)^2 \mathcal{E}_0, \quad (13)$$

where \mathcal{E}_0 is our ability to approximate a transmission matrix with no correction, namely with the ballistic light alone.

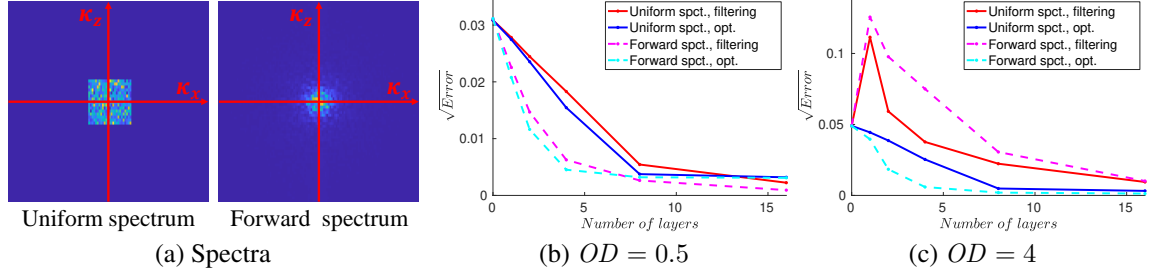


Figure 4: **Numerical simulation:** We synthesize transmission matrices using a very dense multi-layer model and test how well we can fit them with a sparser set of layers. We compare two types of volumes, whose spectra are illustrated in (a). The first one has a random spectrum sampled from a uniform distribution, and the second corresponds to a forward scattering spectrum with more content at the low frequencies. We plot square root of the fitting error as a function of the number of layers, as predicted in claim 1, with a uniform spectrum this decays linearly with the number of layers until we pass the Nyquist limit. The error with the more realistic forward scattering spectrum decays much faster, but analytic characterization is harder. We compute the layers using a naive filtering of the ground truth as well as using gradient decent optimization. The naive filtering provides good results at low optical depths, as illustrated in (b), but fails at higher OD s as illustrated in (c).

Numerical validation: To test the decay of the multi-slice fitting error as a function of the number of layers M , we generated synthetic transmission matrices. We used two types of refractive index volumes, in the first case we selected random values for the spectrum $\hat{n}(\kappa)$, for any frequency $\|\kappa\| \leq \Omega_n$, using a band $\Omega_n = 0.3/\lambda$. The second type of refractive volume $n(\mathbf{r})$ is filled with set of spheres at random positions, each sphere has a random refractive index different than that of the leading medium. This is a more realistic approximation to the structure of real tissue where we have cells with a certain refractive index embedded in a surrounding medium with a different refractive index. In Fig. 4(a) we show a slice through the two spectra $\hat{n}(\kappa)$ we receive, with the random spheres the spectrum decays more naturally, and we have much more content at low frequencies than in high ones. This is a more realistic approximation to the spectrum of real tissue since the fact that tissue is forward scattering implies that its spectrum should have more content at lower frequencies. We start with weakly scattering volumes with a low optical depth value $OD = 0.5$.

We synthesized a target $\mathcal{T}_{\text{exact}}$ matrix using a multi-slice model where the planes are sampled very densely. We generated a set of sparse multi-slice approximations with increasing M values in two ways. First, we use gradient descent optimization to minimize the fitting error in Eq. (11). Second, we use a naive filtering of the ground truth volume, where we simply set to zero any frequency content at κ_z values larger than the possible Nyquist range $\Lambda^M = \frac{M}{d}$. In Fig. 4(b) we plot the square root of the reconstruction error as a function of M and one can see that with a uniform spectrum the square root of the error indeed decays linearly with M , suggesting that the actual reconstruction error decays quadratically with M . The curves reach a plateau when M exceeds the Nyquist requirements. This validates the prediction of claim 1. However, with the more realistic forward scattering volume, the decay of the fitting error is *significantly faster* than the analytic quadratic prediction. For both types of volumes the optimization provides better fits with low M values, but for high M values it runs into local minima and the fitting error it achieves can be higher than the one achieved by naive filtering.

In our plots the case $M = 0$ refers to no correction at all, so effectively we assume that the transmission matrix is diagonal. The similarity between a diagonal transmission matrix and the target transmission matrix is a measure of the amount of ballistic light.

Multiple scattering

The analysis in the previous section has assumed the sample is weakly scattering. While it is hard to give analytical results in the case of multiple scattering, it appears that when the optical depth of the tissue is moderate, light paths undergo a small number of scattering events without being completely scrambled, and the same results hold. The reason is that, since tissue is forward-scattering, light only scatters at small angles. Therefore, after a small number of scattering events, most light paths remain within the butterfly area of the spectrum. This is usually the regime that wavefront-shaping algorithms like Aizik et al. [2022], Aizik and Levin [2024] attempt to tackle as such algorithms attempt to push the depth at which conventional microscopes can see, but they do not yet attempt to image extremely deep where scattering is fully diffused.

To illustrate this, we carry a Monte-Carlo path tracing through a volume. We consider light paths of the form $\vec{\mathbf{r}} = \mathbf{r}_0, \mathbf{r}_1, \dots, \mathbf{r}_\ell$, and denote the direction of the ray between points $\mathbf{r}_k, \mathbf{r}_{k-1}$ by $\vec{\omega}_k$. That is, when a light path scatters at a point \mathbf{r}_k it is changing its direction from $\vec{\omega}_k$ to $\vec{\omega}_{k+1}$, see illustration in Fig. 5(a). This is equivalent to sampling the

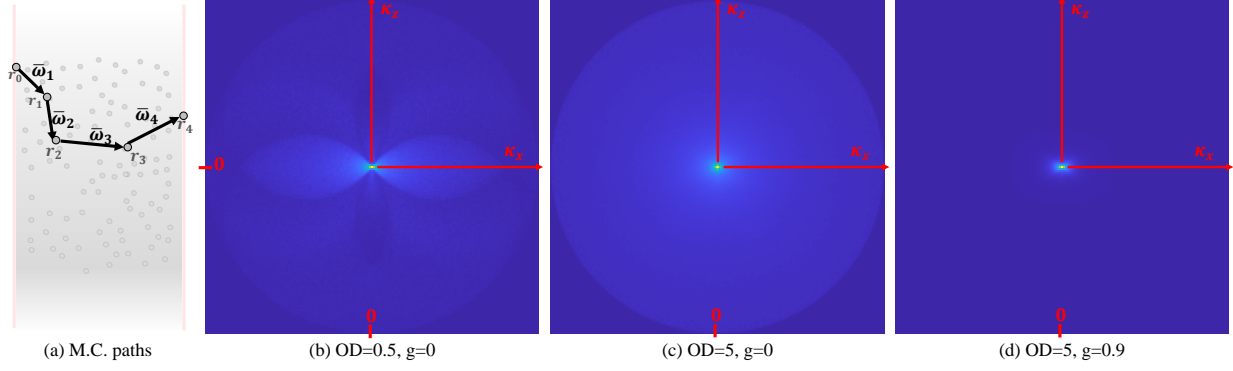


Figure 5: **3D frequencies of MC paths:** (a) An illustration of a Monte-Carlo path in the volume. (b-d) We plot a histogram of the 3D frequencies traced by such paths. (b) A weakly scattering volume of $OD = 0.5$ with an isotropic phase function, shows most frequencies lie inside a narrow butterfly area. (c) When OD is increased to 5 multiple scattering paths generate content at other frequencies. (d) Even at high optical depths, if the phase function is forward scattering as in tissue, most content is at the low frequencies.

3D frequency $\kappa = 1/\lambda(\bar{\omega}_{k+1} - \bar{\omega}_k)$. Our Monte-Carlo simulation samples the first direction on the path anywhere inside the numerical aperture of the expected illumination objective. We sample paths according to a target phase function and optical density but discard all paths that eventually exit the volume at directions outside the numerical aperture as such paths cannot be collected by the imaging objective. However, the inner nodes on the path can include scattering at large angles beyond the NA. After tracing multiple paths through the volume we compute a histogram of the traced 3D frequencies and we visualize a κ_x, κ_z slice through it. In Fig. 5(b-d) we plot a few such histograms. We start by setting the optical depth of the volume to $OD = 0.5$ (Fig. 5(b)), in this case most paths scatter only once and indeed most of the histogram content is inside the butterfly shape of Fig. 3(a). There is some content outside this ellipse since a few of the paths we traced are longer. In Fig. 5(c) we repeated a similar simulation increasing to $OD = 5$, meaning that the average number of scattering events on a path is 5. Such longer paths turn in a variety of directions, and we get content over the entire 3D spectrum. In Fig. 5(b,c) we have assumed that the light is scattering isotropically (Heney-Greenstein parameter $g = 0$). In Fig. 5(d) we repeated the experiments with $OD = 5$ but used a forward scattering phase function which better describes tissue, with a Heney-Greenstein parameter $g = 0.9$. Unsurprisingly, most of the paths traced contribute to *low frequencies*, and even though paths are long, most content is inside the butterfly and not in the area of the missing cone. This observation has a significant impact on the analysis of layered approximations: even if they can only capture the low frequencies of the refractive volume, they can still provide a good approximation to the transmission matrix.

In Fig. 4(c) we numerically tested a multi-slice fitting of a transmission matrix at a larger optical depth, $OD = 4$. All other experimental conditions are equivalent to Fig. 4(b) as described above. With more scattering the naive filtering solution fails for low M values, in the sense that it is worse than an approximation with $M = 0$ layers. This is not surprising since the filtering approach is only valid when the spacing between the layers is lower than the mean-free path of the scattering volume, namely that the light does not scatter more than once between two layers. However, the optimized solution still decreases with M . For a uniform spectrum the optimized solution decreases quadratically with M as predicted in Claim 1 for the weakly scattering case. With a forward scattering spectrum, the decay is much faster.

Transmission matrices under bounded support

Due to the large memory requirements of 4D transmission matrices, they are usually only sampled within a bounded support. That is, we only move illumination point sources inside a small, bounded area of width $\Omega_p \times \Omega_p$, and the number of columns we store in the transmission matrix is limited. To sample the same matrix using directional illumination we should put an aperture before the sample so that the directional beams only propagates through a window of size $\Omega_p \times \Omega_p$, see Fig. 6(a-b).

When fitting layers, we need to account for the fact that a point/plane illumination scattering through a volume is expanding. Thus, the aberration layers required to explain the transmission matrix are wider than the imaged area of width $\Omega_p \times \Omega_p$, leading to discrepancy between the number of constraints and the number of degrees of freedom in the fitted layers. The layer support increases with the sample thickness d . This would imply that when using transmission

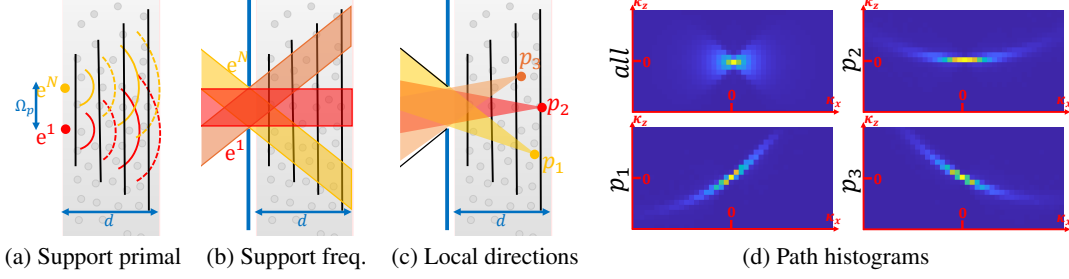


Figure 6: Layer support: (a) as point source expand while propagating through the volume the width of the aberration layers should be wider than the support Ω_p over which the transmission matrix is measured. (b) To express compact support transmission matrices in the Fourier basis, we illuminate the volume by a set of plane waves passing through an aperture. Such waves also expand through the volume to an area wider than the aperture. (c) The local cone of illumination angles reaching different points inside the volume is much smaller than the actual range of incoming illuminations. (d) Since locally each point receives light through a limited angular cone, the local Fourier transform has a lower axial range. To show this we plot the full histogram of angles scanned by Monte-Carlo paths (this is a zoom of the histograms in Fig. 5). We also plot only the histogram of paths passing through the 3 points marked in (c). One can see that such local path-histograms have a limited axial spread. Due to this limited range they can be explained with fewer layers.

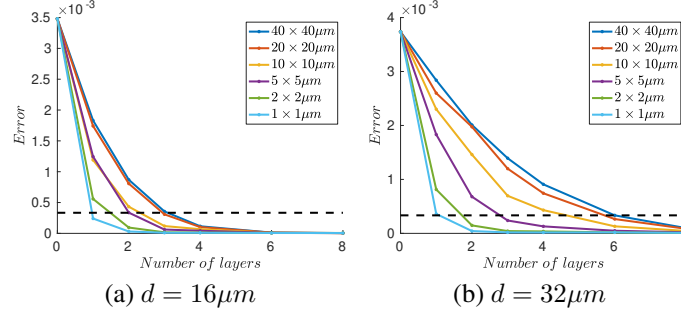


Figure 7: Layer support: We plot fitting error as a function of the number of layers for volumes at two thicknesses. We evaluate fitting while varying the range Ω_p covered by the transmission matrix. Smaller supports can be fitted with fewer layers since the local distribution of illumination angles is smaller, resulting in lower range of axial frequencies.

matrices with a bounded support the layers may allow more over-fitting and hence, we can fit such matrices with a smaller number of layers.

We argue that compact support transmission matrices can indeed be fitted with a sparser set of layers and that this goes beyond over-fitting. To see this we consider Fig. 6(b). Expressing a transmission matrix with a compact support at the frequency basis is equivalent to illuminating the sample with plane waves spanning a wide set of angles, but all the waves pass through a narrow aperture of width Ω_p . In this case most points inside the volume usually do not receive light from all angles. In Fig. 6(c) we plot the narrow cone of angles arriving at three different points (a ray leaving a point p_j at angle $\tilde{\omega}$ is included in the cone only if this angle is not cropped by the aperture at the back of the sample). Since the cone of light reaching each point is narrower than the full numerical aperture, a local Fourier transform would not have content over the full butterfly area, but only cover a lower range of axial ω_z frequencies. Hence, following the analysis in the previous section, it can be sampled with fewer layers.

To illustrate this, we use again Monte-Carlo path tracing. In Fig. 6(d) we plot the histogram of frequencies visited by a M.C. process, but we only record the paths that passed in three local regions marked in Fig. 6(c). Comparing these histograms to the histogram of paths in the entire volume, we see that the local histograms have a much narrower axial range.

Numerical simulation: To test the effect of support on the number of fitted layers we return to the numerical simulation of Fig. 4. To keep within reasonable memory consumption, our simulation used a transmission matrix with $N = 81^2$ columns corresponding to a dense sampling of illumination sources in an area of $\Omega_p \times \Omega_p = 40 \times 40 \mu\text{m}$ at a pitch of $0.5 \mu\text{m}$ under illumination wavelength $\lambda = 0.5 \mu\text{m}$. We simulate two volumes of thicknesses $d = 16 \mu\text{m}$ and $d = 32 \mu\text{m}$ including spheres spread at the same density ($OD = 0.5$ and $OD = 1$ correspondingly). Comparing the fit as a function of the number of layers in Fig. 7 we can see that unsurprisingly we need more layers to explain the thick sample. We

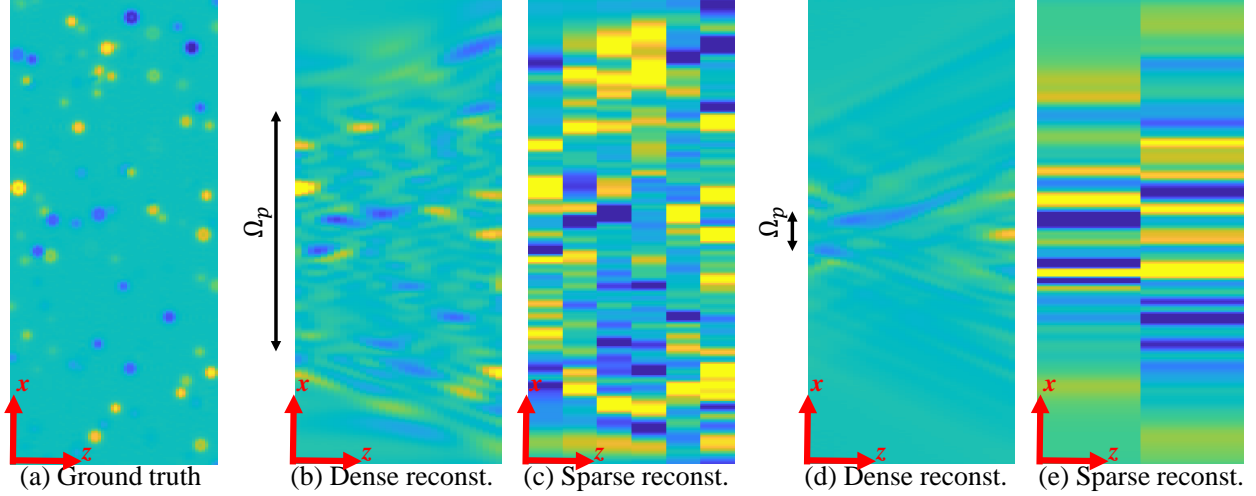


Figure 8: **Reconstructed volume:** (a) An xz slice from a toy volume, visualizing its refractive index variations. (b,d) Two reconstructions of the volume using a dense layer sampling. When the support of the measured window Ω_p shrinks, the lateral extent of the reconstructed region decreases, however, its axial resolution is also reduced. (c,e) A sparse fit with the same input. Despite the low quality of these reconstructions, they predict well the columns of the transmission matrix of the given support Ω_p .

then test the effect of the support, by only fitting subsets of columns contained in smaller Ω_p ranges. One can see that indeed smaller supports can be well-fitted with a smaller number of layers.

As another way to understand it, we show in Fig. 8 an xz slice from the ground truth refractive index volume and from a few reconstructions. We first optimized for a layer fitting with a dense sampling (high layer number M). Even in this case the axial resolution of the reconstruction is poor, and the axial resolution is worse when the support Ω_p is low. This explains why lower supports can be fitted with fewer layers. For each of the two supports we also show a sparse fit, with the minimal M value that provides a good prediction of the transmission matrix.

Implications to layered wavefront shaping systems. Due to the limited memory effect correlation in biological samples, a wavefront shaping system with a single SLM can correct an extremely small region inside the tissue. Ideally, to correct a wide field-of-view we need a volumetric correction whose structure is the conjugate of the phase variation inside the tissue, as in Fig. 1. We would like to approximate such a volumetric correction with a small number of layers implemented by a small number of planar SLMs. In Fig. 7 we plotted some bar below which the approximation is reasonable. We can see that for e.g. the $40 \times 40 \mu m$ support we can obtain good focusing with about $M = 6$ layers. It is likely that fitting a full field-of-view of a few hundred microns would require more layers. However, we can see that while with $M = 1$ layer we could only focus over a small area of about $1 \times 1 \mu m$, when increasing to $M = 2$ we could focus over a $\times 16$ larger area of support $4 \times 4 \mu m$, and with $M = 3$ we could focus over a $\times 100$ larger area of support $10 \times 10 \mu m$. Computing multiple correction elements is only going to increase the complexity of the wavefront shaping algorithm in Aizik and Levin [2024] linearly with the number of layers. Alternatively, a wavefront shaping system using a single SLM would need to scan the field-of-view sequentially and correct each local window independently. Since the increase in the support of the window we can explain with e.g. 3 layers is significantly larger than a $\times 3$ factor, a multi-conjugate wavefront shaping system with a small number of SLMs as in Monin et al. [2022], Thaung et al. [2009], Laslandes et al. [2017], Furieri et al. [2023] can already have a large practical benefit. While Fig. 7 only considers a simulation, we analyze realistic numbers below with a transmission matrix measured from a real tissue sample.

We note that wavefront shaping algorithms like Aizik et al. [2022], Aizik and Levin [2024] perform computation in the optics and they do not need to acquire and store the full transmission matrix in memory, hence the computational constraints of this study do not apply to them.

These results are in agreement with the ones demonstrated and analyzed by recent multi-conjugate Adaptive Optics systems Thaung et al. [2009], Laslandes et al. [2017], Furieri et al. [2023], KAM et al. [2007], Simmonds and Booth [2013], wei Wu and Cui [2015], which correct aberrations through two AO surfaces rather than one. These systems were aimed at correcting aberrations in the optical path, rather than 3D tissue scattering as studied in this paper. However, they demonstrate that the field-of-view which can be corrected by two adaptive optics planes is significantly wider than the one supported by a single such surface.

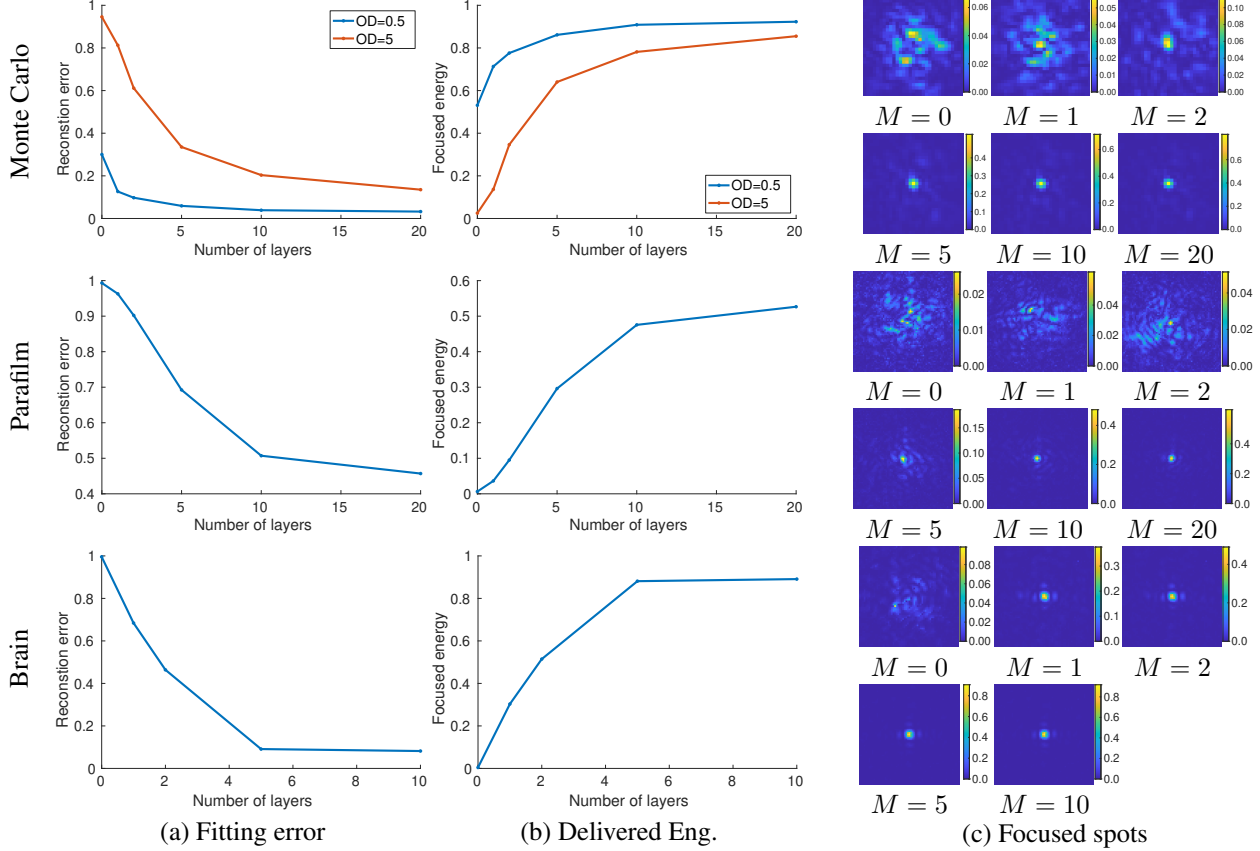


Figure 9: **Fitting transmission matrix:** We fit a few types of transmission matrices with multi-slice model. The top panel tested physically accurate transmission matrices simulated with the Monte-Carlo approach of Bar et al. [2020] at two optical depths. Lower panels used a transmission matrices measured in the lab through layers of paraform and mouse brain. (a) The reduction in fitting error as a function of the number of layers. (b) The averaged delivered energy (correlation between captured and fitted matrices). (c) An example of a spot behind the tissue using the wavefront estimated by the layered model, with different number of layers. (for the M.C. matrices we only show focusing at $OD = 5$).

Compression: Another motivation for approximating transmission matrices with a multi-slice model is to compress a 4D object into a 3D one. Usually, a large compression is possible despite the fact that the layered approximation has a support wider than the area covered by the transmission matrix. To demonstrate some typical numbers, in Table 1 we evaluate the compression ratios corresponding to the different supports in Fig. 7(b). For each support we chose the number of fitted layers, by selecting the lowest number which provides a fitting error below the dashed bar. The compression ratio is equivalent to the ratio between the number of entries in the fitted layers (whose support is wider than the range Ω_p included in the transmission matrix) to the number of entries in the 4D transmission matrix. Clearly the compression is larger for wide supports, but even for small supports there is still a significant gain.

Support	Layer #	3D:4D ratio
$1 \times 1 \mu m$	1	0.0212
$2 \times 2 \mu m$	2	0.0191
$5 \times 5 \mu m$	3	0.0085
$10 \times 10 \mu m$	4	0.0044
$20 \times 20 \mu m$	6	0.0032
$40 \times 40 \mu m$	6	0.0019

Table 1: Compression ratios facilitated when approximating a 4D transmission matrix with planar aberration layers, for the data in Fig. 7(b). For each support we compute the required number of layers according the cut-off dashed bar in Fig. 7(b). While the compression is higher when the transmission matrix covers a large support (and has a lot of columns), even with smaller support the layered models achieve compression.

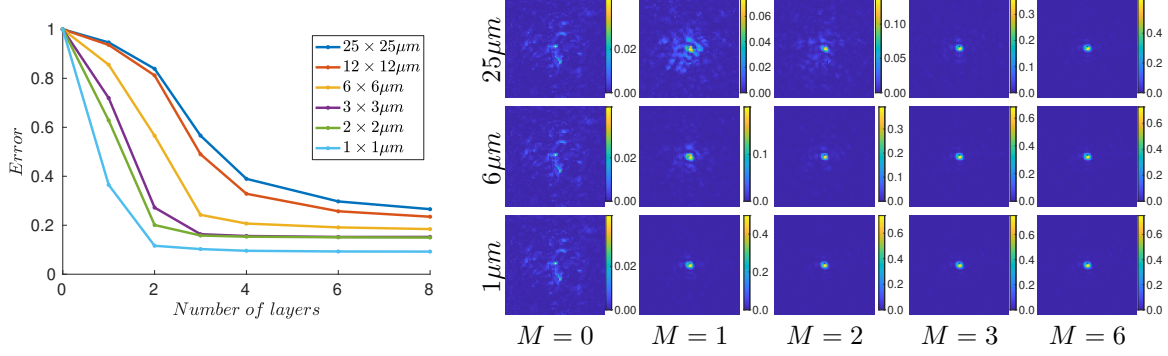


Figure 10: Layer support for a captured transmission matrix: We consider a transmission matrix captured in the lab through a chicken breast layer of thickness $140\mu\text{m}$. Left: plotting fitting error as a function of the number of layers. Smaller supports can be fitted with fewer layers since the layer support is larger relative to Ω_p . Right: illustration of a spot focusing behind the tissue using an increasing number of fitted layers. At the top row we need a larger number of layers, but the spot can be scanned over a $25 \times 25\mu\text{m}$ window using the same layers. In the lower rows we achieve a focused spot using a smaller number of layers but these layers can scan the focused spot over smaller windows of sizes $6 \times 6\mu\text{m}$ and $1 \times 1\mu\text{m}$.

Empirical evaluation of multi-slice approximations

In this section we consider a few transmission matrices and check empirically how well we can approximate them with a multi-slice model. We start with numerically simulated transmission matrices using a more accurate wave-propagation model. We then test lab-captured transmission matrices measuring realistic scattering samples.

While the analysis used the Fourier representation of the transmission matrix, our simulations and measurements use transmission matrices expressed in the primal domain, since in practice, wavefront shaping algorithms use primal measurements.

Monte-Carlo transmission matrices

The transmission matrices used in the simulations of the previous sections were generated using multi-slice models with very dense slices. The multi-slice model is only an approximation to the full wave-equation because it does not simulate back-scattering paths. To test the discrepancy between this model and the full wave equation, we used the Monte-Carlo algorithm of Bar et al. [2019, 2020] to synthesize transmission matrices. It has been shown that this algorithm generates complex fields with physically correct statistics which are equivalent to an exact solution to the wave equation, yet it is much faster to compute and scales to much larger scenes. In particular, the M.C. algorithm simulates scattering from particles at any point in the volume (not only on sparse slices) and at all angles (including back-scattering). We simulated a volume of thickness $d = 50\mu\text{m}$ at $\lambda = 0.5\mu\text{m}$ and illuminated it with point sources spaced over an area of $\Omega_p = 18\mu\text{m}$. We measured the scattered fields over a wider support of $30 \times 30\mu\text{m}$. We used a forward scattering phase function as is common in real tissue. We simulated volumes with two different optical depths and fitted them with a multi-slice model, while increasing the number of layers. The fit results are plotted in Fig. 9(top). The layered transmission matrices have $\times 7$ lower fitting error when compared to the ballistic term alone which is equivalent to fitting with zero layers. However, even when the number of layers increases and approaches the Nyquist limit, the fitting error does not decrease to zero. This failure is a combination of two issues. First, the fact that the actual transmission matrix includes scattering at wide angles which are not modeled by the layered approximation, and second, the fact that the optimization problem is not convex, and the gradient descent does not converge to a global optimum.

As another way to understand the quality of the fit, we tested the correlation between columns of the exact and fitted transmission matrices and measured

$$\mathcal{C}_M = \frac{1}{K} \sum_k \left| \frac{\mathbf{t}_{\text{exact}}^k \cdot \mathbf{t}_{\text{fit},M}^k}{\|\mathbf{t}_{\text{exact}}^k\| \cdot \|\mathbf{t}_{\text{fit},M}^k\|} \right|^2 \quad (14)$$

where $\mathbf{t}_{\text{exact}}^k, \mathbf{t}_{\text{fit},M}^k$ are columns from the input and fitted transmission matrices. This provides a prediction of the percentage of energy we can deliver to a point behind the tissue if we use $\mathbf{t}_{\text{fit},M}^k$ as a wavefront shaping correction, rather than the exact $\mathbf{t}_{\text{exact}}^k$ (note that this only evaluates the energy with respect to the modes included in the input transmission matrix, but there may be additional correction modes not captured by the transmission matrix. Namely, if we would measure a transmission matrix over a wider Ω_p support we could focus more light to a point). With sufficient M values

we can deliver more than 80% of the energy, as plotted in the top row of Fig. 9(b). In Fig. 9(c) we also show some examples of the spot behind the tissue if we use $\mathbf{t}_{\text{fit},M}^k$ as a wavefront shaping correction. For $M \geq 5$ layers the fit is good enough to provide a sharp spot. Note that while we only show focusing at one point, the layers are optimized such that they allow us to focus at *any point* inside the $\Omega_p \times \Omega_p = 18 \times 18 \mu m$ window.

Acquired transmission matrices

We used the Hadamard algorithm of Popoff et al. [2010] to capture transmission matrices of real samples in the lab. We measured a layer of parafilm, and two slices of mouse brain and chicken-breast tissue. We measured the parafilm layer to be of thickness $d = 46 \mu m$, the mice brain to have thickness $400 \mu m$ and the chicken breast to be of thickness $d = 170 \mu m$. The transmission matrices cover an area of $\Omega_p = 25 \mu m$. The measurement is very noisy, mostly due to vibrations during the long capture. Due to the noisy acquisition the fit is not as good as in the synthetic case, but the fitted wavefronts can still focus more than 50% of the energy and generate sharp spots behind the tissue. We show the fits for the parafilm and brain samples in the two lower panels of Fig. 9. We also show the spot we can get behind the tissue using the approximated transmission matrix. Note that these wavefronts are computed numerically, by multiplying the approximated wavefront by the captured transmission matrix.

In Fig. 10 we show fits on the chicken breast matrix. Here we tested the quality of the fit as a function of ranges Ω_p . For that, the algorithm attempts to fit a subset of the measured columns, limited into smaller spatial ranges Ω_p . As in Fig. 7, we see that smaller spatial ranges can be fitted with fewer layers, since if the transmission matrix only covers a limited spatial support, the range of illumination angles reaching each point in the volume is effectively very narrow, hence locally, the Fourier transform has a limited axial range. From the results in Fig. 10 we can see that for the $25 \times 25 \mu m$ support we measured we can obtain good focusing with about 3 – 4 layers. Fitting a full field-of-view of several hundred microns likely requires additional layers. However, we observe that while using $M = 1$ allows us to focus on a small area of about $2 \times 2 \mu m$, with $M = 2$ focus is expanded to a $\times 9$ larger area of $6 \times 6 \mu m$, and with $M = 3$, we can focus on an area $\times 150$ larger, reaching $25 \times 25 \mu m$. Therefore, using multiple layers can significantly accelerates a sequential scanning of a wide field-of-view.

3 Discussion

This paper studies how well we can fit transmission matrices with multi-slice models and how many layers are needed in practice. We show that the required number of layers is much lower than the prediction of Nyquist sampling theory. This is because the missing cone problem of 3D microscopy turns into an advantage when analyzing transmission matrices. Moreover, as tissue is forward scattering its 3D spectrum contains most energy in the low frequencies and much less energy in the higher ones. Hence, even if the sparse sampling low-pass the large axial frequencies not much energy is lost.

We validate this prediction using both synthetic simulations and realistic lab measurements. We show that even though realistic transmission matrices contain backward and side-ward scattering which are not modeled by multi-slice matrices, they provide a reasonable approximation which is good enough for wavefront shaping focusing.

Overall, the findings of our analysis offer a few optimistic predictions. First, transmission matrices can be largely compressed, while transmission matrices are 4D objects, they can be reasonably approximated with 3D layered models. Moreover, multi-slice models can be very applicable for the design of non-local wavefront shaping systems, and we may be able to build a volumetric correction with a small number of layered SLMsThaung et al. [2009], wei Wu and Cui [2015], Laslandes et al. [2017], Furieri et al. [2023]. Even if 2 – 3 SLM layers may not be enough for correcting the full field-of-view of a wide image through a thick tissue, they can allow us to increase the support of the fitted area by much more than $\times 2 - 3$, thus they can significantly accelerate a sequential correction of a wide image.

4 Methods

Mice brain samples used in this manuscript were approved by Institutional Animal Care and Use Committee (IACUC) at the Hebrew University of Jerusalem (MD-20-16065-4).

Volume synthesis

To sample the 3D volumes used to simulate multi-layer transmission matrices we sampled spheres at random positions. We sampled the spheres so that the resulting volume would have a target optical depth OD . To this end we had to select two parameters, the sphere density, and the variation in refractive index induced by the sphere.

The sphere radii were uniformly sampled in the range $0.5 - 1.5\mu m$ (so diameters in the range $1 - 3\mu m$) with illumination wavelength $\lambda = 0.5\mu m$. We note that a sphere with radii ς has a 2D cross section area of $\pi\varsigma^2$. Therefore given a target optical depth OD the average number of spheres in a volume of size $W \times W \times d$ should be

$$OD \frac{W^2}{\int p(\varsigma) \pi \varsigma^2 d\varsigma} \quad (15)$$

where $p(\varsigma)$ is the probability of sampling a sphere with radii ς .

Each sampled sphere is assigned a uniform refractive index n , which differs from the refractive index of the leading medium by a random value in the range

$$[-\alpha, \alpha]. \quad (16)$$

We select α so that the resulting volume meets the target optical depth as explained next. To that end we note that the phase masks ρ_m of the multi-slice model in Eq. (2) are equivalent to the integral of refractive indices variation in a slice of thickness Δ_z around it. As the refractive index variation has a low magnitude we can approximate the phase mask as

$$\rho_m(x, y) = e^{\frac{2\pi i}{\lambda} n(x, y)} \approx 1 - \left(\frac{2\pi n(x, y)}{\lambda} \right)^2 + i \frac{2\pi n(x, y)}{\lambda} \quad (17)$$

We approximate ρ_m as

$$\rho_m(x, y) = \mu + \delta\rho_m(x, y) \quad (18)$$

such that μ is the mean of ρ (which is a real positive scalar) and $\delta\rho_m(x, y)$ is a zero mean residual. We note that the mean μ is effected by the range of refractive indices α in Eq. (16). On the other hand we note that light propagating through M aberration layers maintains a ballistic component attenuated by μ^M . To meet a target optical depth we want $\mu^M = e^{-OD}$. We therefore numerically scan multiple values of α and select the one providing the desired optical depth.

References

- Sam Schott, Jacopo Bertolotti, Jean-Francois Léger, Laurent Bourdieu, and Sylvain Gigan. Characterization of the angular memory effect of scattered light in biological tissues. *Optics Express*, 2015.
- Gerwin Osnabrugge, Roarke Horstmeyer, Ioannis N. Papadopoulos, Benjamin Judkewitz, and Ivo M. Vellekoop. Generalized optical memory effect. *Optica*, 4(8):886–892, July 2017. ISSN 2334-2536. doi:10.1364/optica.4.000886.
- M. Alterman, C. Bar, I. Gkioulekas, and A. Levin. Imaging with local speckle intensity correlations: theory and practice. *ACM TOG*, 2021.
- Chen Bar, Marina Alterman, Ioannis Gkioulekas, and Anat Levin. Single scattering modeling of speckle correlation. In *2021 IEEE International Conference on Computational Photography (ICCP)*, pages 1–16, 2021. doi:10.1109/ICCP51581.2021.9466262.
- Daria Andreoli, Giorgio Volpe, Sébastien Popoff, Ori Katz, Samuel Grésillon, and Sylvain Gigan. Deterministic control of broadband light through a multiply scattering medium via the multispectral transmission matrix. *Scientific Reports*, 5:10347, 2015.
- Stefan Rotter and Sylvain Gigan. Light fields in complex media: Mesoscopic scattering meets wave control. *Rev. Mod. Phys.*, 89:015005, Mar 2017. doi:10.1103/RevModPhys.89.015005. URL <https://link.aps.org/doi/10.1103/RevModPhys.89.015005>.
- S. M. Popoff, A. Aubry, G. Lerosey, M. Fink, A. C. Boccara, and S. Gigan. Exploiting the time-reversal operator for adaptive optics, selective focusing, and scattering pattern analysis. *Phys. Rev. Lett.*, 107:263901, Dec 2011. doi:10.1103/PhysRevLett.107.263901.
- Antoine Boniface, Jonathan Dong, and Sylvain Gigan. Non-invasive focusing and imaging in scattering media with a fluorescence-based transmission matrix. *Nature Communication*, 2020.
- Sylvain Gigan, Ori Katz, et al. Roadmap on wavefront shaping and deep imaging in complex media. *Journal of Physics: Photonics*, 4(4):042501, August 2022. ISSN 2515-7647. doi:10.1088/2515-7647/ac76f9.
- Lei Zhu, Fernando Soldevila, Claudio Moretti, Alexandra d’Arco, Antoine Boniface, Xiaopeng Shao, Hilton B. de Aguiar, and Sylvain Gigan. Large field-of-view non-invasive imaging through scattering layers using fluctuating random illumination. *Nature Communications*, 13:1447, 2022. doi:<https://doi.org/10.1038/s41467-022-29166-y>.

-
- Dror Aizik, Ioannis Gkioulekas, and Anat Levin. Fluorescent wavefront shaping using incoherent iterative phase conjugation. *Optica*, 9(7):746–754, Jul 2022.
- Dror Aizik and Anat Levin. Non-invasive and noise-robust light focusing using confocal wavefront shaping. *Nature communications*, 15(5575), 2024.
- Tomer Yeminy and Ori Katz. Guidestar-free image-guided wavefront shaping. *Science Advances*, 7(21):eabf5364, 2021.
- Brandon Y. Feng, Haiyun Guo, Mingyang Xie, Vivek Boominathan, Manoj K. Sharma, Ashok Veeraraghavan, and Christopher A. Metzler. Neuws: Neural wavefront shaping for guidestar-free imaging through static and dynamic scattering media. *Science Advances*, 9(26):eadg4671, 2023.
- Sungsam Kang, Seungwon Jeong, Wonjun Choi, Hakseok Ko, Taeseok D. Yang, Jang Ho Joo, Jae-Seung Lee, Yong-Sik Lim, Q-Han Park, and Wonshik Choi. Imaging deep within a scattering medium using collective accumulation of single-scattered waves. *Nature Photonics*, 9(4):253–258, March 2015. ISSN 1749-4893. doi:10.1038/nphoton.2015.24.
- Baptiste Blochet, Kelly Joaquina, Lisa Blum, Laurent Bourdieu, and Sylvain Gigan. Enhanced stability of the focus obtained by wavefront optimization in dynamical scattering media. *Optica*, 2019.
- Christopher Metzler, Manoj Sharma, Sudarshan Nagesh, Richard Baraniuk, Oliver Cossairt, and Ashok Veeraraghavan. Coherent inverse scattering via transmission matrices: Efficient phase retrieval algorithms and a public dataset. *IEEE ICCP*, pages 1–16, 2017. doi:10.1109/ICCPHOT.2017.7951483.
- Manoj Sharma, Christopher Metzler, Sudarshan Nagesh, Oliver Cossairt, Richard Baraniuk, and Ashok Veeraraghavan. Inverse scattering via transmission matrices: Broadband illumination and fast phase retrieval algorithms. *IEEE Transactions on Computational Imaging*, 6:95–108, 2020. doi:10.1109/TCI.2019.2919257.
- Ye Ryoung Lee, Dong Young Kim, Yonghyeon Jo, Moonseok Kim, and Wonshik Choi. Exploiting volumetric wave correlation for enhanced depth imaging in scattering medium. *Nature communications*, 14(1), December 2023. ISSN 2041-1723.
- YoonSeok Baek, Hilton B. de Aguiar, and Sylvain Gigan. Phase conjugation with spatially incoherent light in complex media. *Nature Photonics*, 17(12):1114–1119, July 2023. ISSN 1749-4893.
- Yiwen Zhang, Minh Dinh, Zeyu Wang, Tianhao Zhang, Tianhang Chen, and Chia Wei Hsu. Deep imaging inside scattering media through virtual spatiotemporal wavefront shaping. *arXiv preprint arXiv:2306.08793*, 2024.
- Roarke Horstmeyer, Jaebum Chung, Xiaozhe Ou, Guoan Zheng, and Changhuei Yang. Diffraction tomography with fourier ptychography. *Optica*, 3(8):827–835, Aug 2016.
- Shwetadwip Chowdhury, Michael Chen, Regina Eckert, David Ren, Fan Wu, Nicole Repina, and Laura Waller. High-resolution 3d refractive index microscopy of multiple-scattering samples from intensity images. *Optica*, 6(9): 1211–1219, Sep 2019.
- Michael Chen, David Ren, Hsiou-Yuan Liu, Shwetadwip Chowdhury, and Laura Waller. Multi-layer born multiple-scattering model for 3D phase microscopy. *Optica*, 7(5):394–403, May 2020.
- Kevin C. Zhou and Roarke Horstmeyer. Diffraction tomography with a deep image prior. *Opt. Express*, 28(9): 12872–12896, Apr 2020.
- Sungsam Kang, Yongwoo Kwon, Hojun Lee, Seho Kim, Jin Hee Hong, Seokchan Yoon, and Wonshik Choi. Tracing multiple scattering trajectories for deep optical imaging in scattering media. *Nature communications*, 14(1), December 2023. ISSN 2041-1723.
- Renhao Liu, Yu Sun, Jiabei Zhu, Lei Tian, and Ulugbek Kamilov. Recovery of continuous 3d refractive index maps from discrete intensity-only measurements using neural fields. *Nat Mach Intell.*, (12):781–791, 2022.
- Yi Xue, David Ren, and Laura Waller. Three-dimensional bi-functional refractive index and fluorescence microscopy (brief). *Biomed. Opt. Express*, 13(11):5900–5908, Nov 2022.
- Renzhi He, Yucheng Li, Junjie Chen, and Yi Xue. Fluorescence diffraction tomography using explicit neural fields, 2024. URL <https://arxiv.org/abs/2407.16657>.

-
- Ulugbek S. Kamilov, Ioannis N. Papadopoulos, Morteza H. Shoreh, Alexandre Goy, Cedric Vonesch, Michael Unser, and Demetri Psaltis. Learning approach to optical tomography. *Optica*, 2(6):517–522, Jun 2015.
- Yu Sun, Zhihao Xia, and Ulugbek S. Kamilov. Efficient and accurate inversion of multiple scattering with deep learning. *Opt. Express*, 26(11):14678–14688, May 2018.
- Jörgen Thau, Per Knutsson, Zoran Popovic, and Mette Owner-Petersen. Dual-conjugate adaptive optics for wide-field high-resolution retinal imaging. *Opt. Express*, 17(6):4454–4467, Mar 2009.
- Tsai wei Wu and Meng Cui. Numerical study of multi-conjugate large area wavefront correction for deep tissue microscopy. *Opt. Express*, 23(6):7463–7470, Mar 2015.
- Marie Laslandes, Matthias Salas, Christoph K. Hitzenberger, and Michael Pircher. Increasing the field of view of adaptive optics scanning laser ophthalmoscopy. *Biomed. Opt. Express*, 8(11):4811–4826, Nov 2017.
- T. Furieri, A. Bassi, and S. Bonora. Large field of view aberrations correction with deformable lenses and multi conjugate adaptive optics. *Journal of Biophotonics*, 16(12):e202300104, 2023.
- Jerome Mertz. *Introduction to optical microscopy*. Cambridge University Press, 2019.
- Sagi Monin, Aswin Sankaranarayanan, and Anat Levin. Exponentially-wide etendue displays using a tilting cascade. *IEEE ICCP*, pages 1–12, 08 2022.
- ZVI KAM, PETER KNER, DAVID AGARD, and JOHN W. SEDAT. Modelling the application of adaptive optics to wide-field microscope live imaging. *Journal of Microscopy*, 226(1):33–42, 2007. doi:<https://doi.org/10.1111/j.1365-2818.2007.01751.x>. URL <https://onlinelibrary.wiley.com/doi/abs/10.1111/j.1365-2818.2007.01751.x>.
- Richard D Simmonds and Martin J Booth. Modelling of multi-conjugate adaptive optics for spatially variant aberrations in microscopy. *Journal of Optics*, 15(9):094010, sep 2013. doi:10.1088/2040-8978/15/9/094010. URL <https://dx.doi.org/10.1088/2040-8978/15/9/094010>.
- Chen Bar, Ioannis Gkioulekas, and Anat Levin. Rendering near-field speckle statistics in scattering media. *ACM TOG*, 2020.
- Chen Bar, Marina Alterman, Ioannis Gkioulekas, and Anat Levin. A monte carlo framework for rendering speckle statistics in scattering media. *ACM TOG*, 2019.
- S. M. Popoff, G. Lerosey, R. Carminati, M. Fink, A. C. Boccaro, and S. Gigan. Measuring the transmission matrix in optics: An approach to the study and control of light propagation in disordered media. *Physical Review Letters*, 104(10):100601, March 2010. ISSN 1079-7114. doi:10.1103/physrevlett.104.100601.

Acknowledgments

AL thanks the European Research Council [101043471] for funding this research.

Appendix

Deriving the multi-slice fitting error

Below we prove the claim from the main paper, predicting the decay of the fitting error with the number of layers.

Claim 1 *The reconstruction error of a transmission matrix corresponding to a band-limited weakly scattering volume is bounded by*

$$\mathcal{E}_M \leq \left(\frac{M^* - M}{M^*} \right)^2 \mathcal{E}_0, \quad (19)$$

where \mathcal{E}_0 is our ability to approximate a transmission matrix with no correction, namely with the ballistic light alone, and M^* is the number of layers required for an error-free fitting meeting the Nyquist limit.

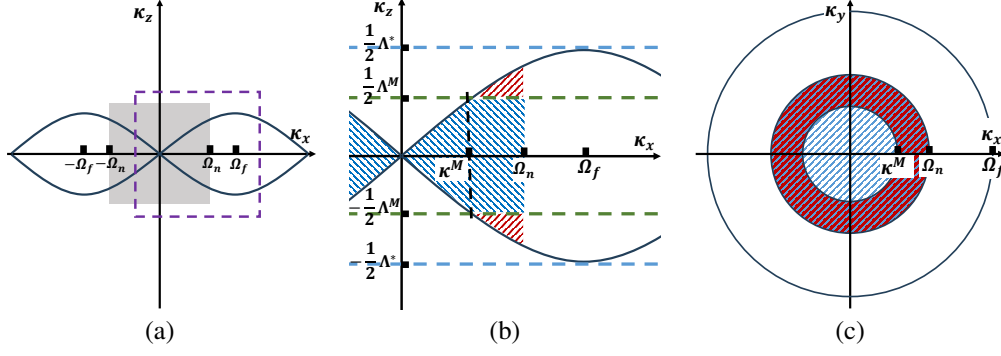


Figure 11: **Spectrum structure:** (a) an $x - z$ slice out of the spectrum of $\hat{n}(\omega)$. Entries of the transmission matrix limited by an aperture \mathbf{NA} only lie inside the butterfly area. We also assume the content of $\hat{n}(\omega)$ is limited to a band of support Ω_n marked in gray in the figure. (b) zooming on the center right area of (a) (purple rectangle), assuming the ω_z axis is cut at $\pm \frac{1}{2}\Lambda$, the transmission matrix entries inside the dashed blue area are maintained, and the entries in the dashed red area are lost. The approximation error with M layers is proportional to the red volume, which is shown to scale quadratically with M . (c) The $x - y$ projection of the maintained/lost areas.

Proof: To prove this result we use a brute-force selection of the layers ρ_1, \dots, ρ_M . We simply set to zero any frequency content of the refractive volume $\hat{n}(\kappa)$ at $|\kappa_z|$ values larger than the possible Nyquist range

$$\Lambda^M = \frac{1}{\Delta_z} = \frac{\lambda M}{d}, \quad (20)$$

and we then Fourier transform $\hat{n}(\kappa)$ to \mathbf{n} and sample planes at spacing Δ_z . In the following paragraphs we offer an upper-bound calculation of the number of transmission matrix entries that lie outside the band Λ^M and are hence lost by the low-pass operation. We show this scales quadratically with M .

To perform this calculation we consider Fig. 11. We note that the butterfly shape is such that low 2D frequencies (i.e. low $|\kappa_{xy}|$) also span less content in the κ_z axes, and hence these frequencies are not lost even with low bandwidths Λ . For the higher $|\kappa_{xy}|$ frequencies, the lower κ_z part marked in blue is preserved, while the higher portion marked in red in Fig. 11(b) is lost. Below we preform a conservative calculation of how many transmission matrix entries are included in the red area, and show that this number is bounded by a quadratic function of $(M^* - M)$. Using the assumption that the frequency content of the volume is smaller than the cut-off frequency set by the numerical aperture ($\Omega_n < \Omega_f$) we can approximate the butterfly boundaries at areas where the volume has content as linear curves:

$$|\kappa_z| \leq \mathbf{NA} |\kappa_{xy}|. \quad (21)$$

Also, if $\Omega_n < \Omega_f$ the maximal κ_z frequency at which we observe content does not get to $\mathbf{NA}\Omega_f/2$ as derived in Eq. 8 of the main paper, but can be actually reduced to $\mathbf{NA}\Omega_n$. Thus, for error-free reconstruction it is enough to maintain content up to a cut-off frequency of

$$\frac{1}{2}\Lambda^* = \mathbf{NA}\Omega_n, \quad (22)$$

and as a result the minimal number of required layers is

$$M^* = 2\mathbf{NA}\Omega_n d \quad (23)$$

With this model we treat the red area as a triangle, and we denote the frequency at which the triangle intersects with the z -axis bandwidth as κ^M , it can be shown that

$$\kappa^M = \frac{\Lambda^M}{2\lambda\mathbf{NA}} = \frac{M}{2\mathbf{NA}d}. \quad (24)$$

To compute the number of transmission matrix entries in the red region, we need to compute an integral of the following form

$$\int_{\kappa=\kappa^M}^{\Omega_n} \mathbf{NA}(\kappa - \kappa^M) \cdot (2\pi\kappa) \cdot f(\kappa) d\kappa. \quad (25)$$

The first term in this integral is the distance of the triangle from the cutoff frequency (the triangle at frequency $|\kappa_{xy}| = \kappa$ spans κ_z values in a range from $\mathbf{NA}\kappa^M$ to $\mathbf{NA}\kappa$), the 2nd term encodes the fact that in the 3D Fourier domain there is a

full circle of frequencies with norm $|\kappa_{xy}| = \kappa$. Finally the function $f(\kappa)$ encodes the density of transmission matrix entries which are mapped to frequency $\kappa = (\kappa_x, \kappa_y, \kappa_z)$. Below we show this is bounded by

$$f(\kappa) \leq \frac{c}{|\kappa_{xy}|} \quad (26)$$

where c is a constant scalar. With this we can bound the volume of missing frequencies as

$$\int_{\kappa=\kappa^M}^{\Omega_n} \mathbf{NA}(\kappa - \kappa^M) \cdot (2\pi) \cdot c d\kappa = \mathbf{NA}\pi c (\Omega_n - \kappa^M)^2 \quad (27)$$

By plugging Ω_n from Eq. (23), and the value for κ^M as in Eq. (24) we get that the density of transmission matrix entries in the filtered red volume is proportional to

$$\int_{\omega=\omega^M}^{\frac{1}{2}\Omega_n} \mathbf{NA}(\omega - \omega^M) \cdot (2\pi) \cdot c d\omega \propto (M^* - M)^2. \quad (28)$$

Using the same reasoning when we have $M = 0$ layers the error in reconstructing the transmission matrix, namely the full volume of the butterfly shape is proportional $(M^*)^2$. This leads us to the desired Eq. (19).

The last thing we need to prove is that the density of transmission matrix entries around the 3D frequency $\kappa = (\kappa_x, \kappa_y, \kappa_z)$ is bounded by

$$f(\kappa) \leq \frac{c}{|\kappa_{xy}|} \quad (29)$$

For that we recall that we sample a frequency κ when we have illumination and viewing directions whose frequencies satisfy $\bar{\kappa}^i - \bar{\kappa}^v = \kappa$, where $\bar{\kappa}^i = 1/\lambda\bar{\omega}^i$, $\bar{\kappa}^v = 1/\lambda\bar{\omega}^v$, so $\bar{\kappa}^i, \bar{\kappa}^v$ are vectors of norm $1/\lambda$. For that consider illumination and viewing directions which we parameterize using a 2nd order approximation as

$$\bar{\kappa}^i = \begin{pmatrix} \tau_x + \kappa_x \\ \tau_y + \kappa_y \\ \frac{1}{\lambda} - \frac{\lambda}{2}((\tau_x + \kappa_x)^2 + (\tau_y + \kappa_y)^2) \end{pmatrix} \quad (30)$$

$$\bar{\omega}^v = \begin{pmatrix} \tau_x \\ \tau_y \\ \frac{1}{\lambda} - \frac{\lambda}{2}(\tau_x^2 + \tau_y^2) \end{pmatrix} \quad (31)$$

The difference between these two vectors in the first two coordinates is κ_x, κ_y . The difference in the 3rd coordinate can be expressed as

$$\kappa_z = \lambda(\tau_x\kappa_x + \tau_y\kappa_y) - \frac{\lambda}{2}|\kappa_{xy}|^2 = \lambda((\tau_x, \tau_y) \cdot (s^1|\kappa_{xy}|)) - \frac{\lambda}{2}|\kappa_{xy}|^2 \quad (32)$$

where in the right hand side of the above equation we use the 2D unit norm vector $s^1 = (\kappa_x, \kappa_y)/|\kappa_{xy}|$. With this notation we see that to get the 3D frequency κ_z we need to use viewing directions whose τ_x, τ_y satisfy the linear constraint

$$((\tau_x, \tau_y) \cdot s^1) = \frac{1}{|\kappa_{xy}|} \left(\kappa_z + \frac{1}{2}|\kappa_{xy}|^2 \right). \quad (33)$$

The density of directions satisfying this constraint scales as $1/|\kappa_{xy}|$.

□